School of Natural Sciences and Mathematics

2012-2-1

Sensitivity of Estimated Elastic Moduli to Completeness of Wave Type, Measurement Type, and Illumination Apertures at a Receiver in Multicomponent VSP Data

Herurisa Rusmanugroho and George A. McMechan

GEOPHYSICS. VOL. 77, NO. 1 (JANUARY-FEBRUARY 2012); P. R1–R18, 14 FIGS.
10.1190/GEO2010-0410.1

Sensitivity of estimated elastic moduli to completeness of wave type, measurement type, and illumination apertures at a receiver in multicomponent VSP data

Herurisa Rusmanugroho[1] and George A. McMechan[1]

ABSTRACT

Inversion of phase slowness and polarization vectors measured from multicomponent vertical seismic profile data can yield estimates of all 21 density-normalized elastic moduli for anisotropic elastic media in the neighborhood of each 3C geophone. Synthetic test data are produced by direct evaluation of the Christoffel equation, and by finite-difference solution of the elastodynamic equations. Incompleteness of the data, with respect to illumination (polar and azimuth angle) apertures (qP and/or qS) wave types, wave-propagation directions, and the amount of data (e.g., with or without horizontal slowness components), produces solutions with variations in quality, as revealed by the distribution of model parameter correlations. In a good solution, with all parameters well constrained by the data, the correlation matrix is diagonally dominant. qP-only and qS-only solutions typically produce complementary distributions in their correlation matrices, as they are orthogonal in their sampling of the medium with respect to polarization. The elastic moduli become less independent as the data apertures decrease. If the other input data are relatively complete, the horizontal components of the slowness vector are not needed as the information they contain is redundant. The main consequence of omitting horizontal slowness components is slower convergence. When modest amounts of random noise are added to the slowness and polarization data, in otherwise adequately sampled apertures, the solution is still very close to the correct model, but with larger residual variance.

INTRODUCTION

General anisotropy, parameterized by 21 density-normalized elastic moduli, provides a comprehensive characterization of an anisotropic elastic medium, from the measured polarizations and phase slowness vectors of propagating waves. Below, the terms modulus and moduli should everywhere be understood to be density-normalized, and hence have units of velocity^2 (km^2/s^2). Methods of extracting local anisotropy information can be grouped into phase slowness methods, or slowness + polarization methods. The phase slowness methods include Miller and Spencer (1994), who show an exact inversion from qP or qS data, assuming that the axial shear velocity is known, Miller et al. (1994) who show a field application to a marine walkaway vertical seismic profile (VSP), and Horne et al. (2008) who extend it to 3D. The slowness + polarization methods include de Parscau and Nicloetis (1989), Hsu et al. (1991), and Leaney and Hornby (2007), and Grechka and Mateeva (2007). VSP data are commonly used for inversion for anisotropic moduli as the VSP geometry provides wider propagation angle apertures than surface survey data for the same offset, and wide azimuth apertures. Maximizing angular recording apertures is important because inversion for all 21 elastic moduli requires that the anisotropic medium be sampled by waves propagating in many independent directions; 3C geophones in a borehole can record waves in all incident directions.

Both theoretical and experimental approaches for calculating the 21 independent moduli have been proposed by previous authors. Arts et al. (1992) solve the Christoffel equation, by generalized linear inversion, for the moduli in terms of polarizations and phase velocties. Arts and Rasolofosaon (1992) expand the method to the complex moduli of a general viscoelastic anisotropic medium. Vestrum (1994) performs a least-squares inversion for the best fit to

Manuscript received by the Editor 15 December 2010; revised manuscript received 7 September 2011; published online 1 February 2012.
[1]The University of Texas at Dallas, Center for Lithospheric Studies, Richardson, Texas, USA. E-mail: heru@utdallas.edu; mcmec@utdallas.edu.

the observed group and phase velocities from laboratory measurements; the group velocity inversion is computationally more difficult and its result is less accurate than that based on the phase velocity; below, we use phase velocities only. Dellinger et al. (1998) improve and stabilize Vestrum's algorithm by parameterizing the elastic modulus matrix using eigenstiffnesses and eigentensors, as described by Helbig (1994).

Many inversion algorithms and examples of inversion of VSP data can be found in the literature (e.g., Bona and Slawinski, 2008; Kochetov and Slawinski, 2009). Most have restrictions with regard to polar and azimuth angle apertures in the data, are limited in the wave types considered (usually qP waves), or measurement type (polarization or phase slowness vectors, or both). For example, van Buskirk et al. (1986), Norris (1989) and Ditri (1994) assume homogeneity. Horne and Leaney (2000) invert qP and qSV polarization and slowness component measurements obtained from a walkway VSP experiment in the Java Sea region using an adaptive simulated annealing to minimize the misfit function over Thomsen-like parameters and phase velocities for a VTI model. Zheng and Pšenčík (2002) assume arbitrary anisotropy symmetry and invert the polarization vector and the vertical component of the slowness vector of the qP-wave to determine locally weak anisotropy parameters; as horizontal components of the slowness vector are not independent of polarization, the former can be substituted by the latter, and the solution is relatively insensitive to the structural complexities in the overburden.

Dewangan and Grechka (2003) provide procedures to estimate all 21 moduli from 9C VSP data by solving the Christoffel equation. Gomes et al. (2004) apply an approach, similar to that of Zheng and Pšenčík (2002), to walkway VSP data acquired in the Java Sea region (Horne and Leaney, 2000), and show that the area is neither isotropic nor VTI, but are not able to establish the symmetry of the medium because only qP-wave data along one radial line of sources are used. They also show that slowness vector components estimated from downgoing waves are more accurate than those from upgoing, for qP and qS waves.

Each of the above studies is limited in certain ways by the survey geometry, data apertures, the wave types, or the model parameterization. The effects of these limitations on information content and its distribution in the data have implications for experiment design and the ability for subsequent recovery of elastic moduli. A few papers, notably Norris (1989), Jech (1991), Ditri (1994), and Dewangan and Grechka (2003) have made significant analyses and provide technology for systematic investigation of these relations, but the task is far from complete.

The distribution of information in the data is an important consideration in optimizing data acquisition. Ditri (1994) shows that 15 of the 21 elastic moduli can be determined from data in a single recording plane, and 20 can be determined from data in two planes, provided that the angular apertures are sufficient; theoretically, slowness and polarization components of qP and qS waves measured in only six optimally chosen wave-propagation directions are enough to determine all 21 moduli (Norris, 1989). Unfortunately, these optimal directions are not known a priori, so many more measurements always have to be made in practice.

Jech (1991) shows that a qP wave velocity depends on each of 21 the elastic moduli with sensitivity depending on the propagation direction, so it is theoretically possible to solve for all the 21 moduli from qP data alone, provided that the data apertures are sufficiently wide. However, Jech also points out that if a linearized solution is used, then only nine independent moduli are uniquely recoverable; the others appear in six composite parameters, each of which is a combination of two. Adding qS data (e.g., Dewangan and Grechka, 2003) or solving the nonlinear problem resolves these limitations. Gomes et al. (2004) take a different approach; they restructure the inversion by expressing the two horizontal slowness components in terms of polarizations so the former are only implicitly included.

Given that the anisotropic symmetry and orientation are not known a priori, in this paper, we perform linearized inversions for 21 elastic moduli for a variety of data subsets for a single model, to illustrate how various amounts and types of data incompleteness influence the ability to recover the elastic moduli. The inversions are based on the Christoffel equation (e.g., Ditri, 1994; Dewangan and Grechka, 2003), which is the relation between the measured slowness and polarization components (as a function of direction, for qP, qS1, and qS2 waves), and the elastic moduli. We specifically consider solutions for 21 elastic moduli using wide and limited ranges of polar and azimuth angles, with and without noise, with approximate and with no horizontal slowness components, and for qP waves only and qS waves only. Parameter correlation matrices computed from the Jacobian at convergence assist in evaluation the quality of the solutions, and reveal the number of independent parameters that are recovered from the various subsets of the data. Certainly the inversions would be more efficient if the anisotropy symmetry was known a priori so that the model parameterization could be optimized. Examples are constructed directly from the Christoffel equation, and also from slowness and polarization components measured from synthetic 3D, 9C elastic data.

The elastic moduli have embedded in them, information on lithology, fluid content, fracture orientation and density, and the anisotropy symmetry. Recovery of the elastic moduli is the first step in estimating the petrophysical properties for potential use in production strategy, time-lapse fluid replacement monitoring, and hydraulic fracture evaluation.

METHODOLOGY

In anisotropic media, wave-propagation velocities are a function of direction, wave type, and the elastic moduli. For a given propagation direction (defined by a polar angle and azimuth), the Christoffel equation (Appendix A) produces three sets of the phase velocities and polarizations corresponding to the P-wave, and two S-waves. In anisotropic media, there are quasi-P (qP), faster quasi-S1 (qS1), and slower quasi-S2 (qS2) modes which are not purely longitudinal or shear (Tsvankin, 2001). The Christoffel equation is obtained by substituting a harmonic plane wave into the elastodynamic equation; thus it is a plane wave approximation (Tsvankin, 2001), and so works best at sufficiently large distances from the source that the wavefront curvature is negligible.

Phase slowness and polarization vector data

Inputs to inversion for elastic moduli consist of components of phase slowness and polarization vectors for qP, qS1, and qS2 waves incident at a 3C borehole geophone. The depth derivative dt/dz of the traveltime t in the vertical direction z is the vertical component of the phase slowness vector at the current receiver; this vertical slowness is local and so is independent of the overburden. The vertical phase slowness range is sampled by repeating for all azimuths and offsets for sources at the surface. The horizontal phase slownesses cannot be measured in a vertical hole, and so may be approximated if the overburden is homogeneous, by invoking reciprocity by selecting pairs of sources at the surface, for a fixed receiver in the borehole (Gaiser, 1990). The horizontal components of the slowness vector measured at the surface are the same as those at a fixed receiver in the borehole for a laterally homogeneous (e.g., VTI) medium. If the overburden is not homogeneous, reciprocity is not maintained (e.g., Grechka and Mateeva, 2007), and horizontal slowness components determined at the surface will not be reliable. Taking local horizontal spatial derivatives dt/dx and dt/dy gives components of the phase (not group) slowness vector (Gaiser, 1990; Dellinger, 1991). This is important as the Christoffel equation requires phase slowness components.

The vertical component of slowness and all the polarization measurements are local to the 3C borehole geophone (within 1–2 wavelengths; Nistala and McMechan, 2005). The measurements and the inverted moduli apply only to the neighborhood of the geophone. If horizontal slowness components are approximated by measurements across sources at the surface (Gaiser, 1990), the approximation gets poorer as the complexity of the overburden structure increases (Dewangan and Grechka, 2003; Nistala and McMechan, 2005). The incident angle will be affected by the actual propagation path in complicated structure in the overburden, but the slowness and polarization vector for each arrival will be locally consistent at the geophone, and that is the input data for inversion.

Similarly, all three components of polarization can be measured by a single 3C borehole geophone. The 3C polarizations for qP, qS1, and qS2 waves are obtained by singular value decomposition (SVD) and Alford rotation as summarized by Michaud (2001). The polarization vectors are required to be normalized for input to the Christoffel equation (Appendix A).

Inversion

The inverse problem (Appendix B) of estimating elastic moduli from polarization and slowness vectors (e.g., Dewangan and Grechka, 2003) is also based on the Christoffel equation. We implement the inverse problem with the iterative Levenberg-Marquardt algorithm (e.g., Menke, 1989). Moré's (1977) modification to the Levenberg-Marquardt method is robust, efficient, and shows strong convergence properties. The model parameter vector at iteration $n+1$ is

$$\mathbf{m}_{n+1} = \mathbf{m}_n + [\mathbf{J}_n^{\mathrm{T}}\mathbf{J}_n + \epsilon^2\mathbf{I}]^{-1}\mathbf{J}_n^{\mathrm{T}}\mathbf{K}_n(\mathbf{d}^{\mathrm{obs}} - \mathbf{d}_n^{\mathrm{cal}}), \quad (1)$$

where $\mathbf{m}$ is the model parameter vector and $\mathbf{d}$ is the data vector. The model parameter vector contains the density-normalized elastic moduli, and the data vector contains the polarizations and slownesses for each of the qP, qS1, and qS2 waves. $\mathbf{J}$ is a Jacobian matrix containing the first derivatives of the Christoffel equation with respect to the model vector, and $\mathbf{K}$ is a diagonal matrix containing the derivative of the Christoffel equation with respect to the data vector. ϵ is a damping factor used to avoid local minima, and $\mathbf{I}$ is an identity matrix. Superscripts -1 and T denote inverse and transpose operations, respectively. Superscripts "obs" and "cal" denote the observed and calculated data, respectively. The solution is obtained by minimizing the objective function of the root mean square misfit

$$\Phi_{\mathrm{rms}} = \sqrt{\frac{1}{\mathrm{N}}\sum_{i=1}^{\mathrm{N}}(d_i^{\mathrm{obs}} - d_i^{\mathrm{cal}})^2}, \quad (2)$$

between the observed and calculated slowness and polarization vectors, where N is the number of observed data.

Parameter covariance and the model correlation matrix

Covariance measures how two parameters change together. The larger the magnitude of a covariance, the stronger the relationship between the corresponding model parameters. Normalizing the covariance matrix elements by the product of the standard deviations of the corresponding model parameters gives the correlation matrix (e.g., Rodgers and Nicewander, 1988; Menke, 1989). Menke (1989) shows that the normalized covariance matrix of the model parameters also defines the error amplification resulting from mapping the data into the model. The correlation matrix for an estimated model is a numerical tool that can be used in experiment design even before acquiring data (Menke, 1989) because it is independent of the actual magnitudes and variances contained in the data. The correlation matrix can be calculated from the Jacobian of the inversion at any iteration, but the most salient information is at convergence.

An ideal inverse problem is parameterized in terms of, and solved for, parameters that are independent of each other. In the present context, there are potentially 21 independent moduli. If the inverse problem is well-posed, the solution converges to a model that is close to the correct model, the normalized covariance matrix will be a unit diagonal matrix, interpreted as having no correlation between the estimated moduli. If the problem was not correctly parameterized and the parameters are interdependent, this will manifest as nonzero amplitudes in off-diagonal locations in the correlation matrix (where the row and column indices indicate the parameters that are correlated). Correlations can be positive or negative, and range between -1 and $+1$. So the quality of an inversion can be ascertained by viewing the pattern in the correlation matrix. We identify three main situations; for independent parameters, for interaction between parameters, and for unsolved parameters, depending on the information that is recoverable from the data that are available. This is a key component of the analysis of the examples below.

GENERATION OF SYNTHETIC DATA FOR INVERSION EXAMPLES

Winterstein (1990) notes that a triclinic model with 21 independent elastic moduli can be generated by adding a third set of cracks into a model with monoclinic symmetry, if the normal to the added crack set is neither parallel, nor perpendicular to, the normals of the two crack planes in the host monoclinic medium. The monoclinic symmetry itself can be defined by two crack sets with different crack density, whose normals make an angle of neither 0° nor 90° with each other.

Elastic moduli for a triclinic medium are calculated using the high-order T-matrix model (Jakobsen et al., 2003) to represent the contributions of cracks and their interactions. The elastic moduli for the isotropic host rock are given in equation C-1. The seismic properties of the host rock and of the gas contained in the cracks in the model are from Maultsch et al. (2003). The T-matrix crack parameters (with a crack aspect ratio of 0.05 and an aspect ratio of the crack distribution of 0.1), are the same for all the crack sets. Figure 1 shows the triclinic crack geometry distribution used, in Cartesian coordinates; the crack sets 1, 2, and 3 have crack densities of 0.03, 0.04, and 0.02, respectively. For clarity, each crack set is represented by only a single plane in Figure 1. The corresponding matrix of density-normalized elastic moduli ($\mathrm{km}^2/\mathrm{s}^2$) specifying a homogeneous triclinic medium used for the generation of the synthetic "observed" data is given in equation C-2.

The synthetic examples below are divided into two groups; all use the same modulus model. The first group uses multicomponent, multiazimuth examples generated using deterministic forward modeling of polarization and slowness vectors calculated directly by the Christoffel equation. The second group uses polarization and slowness components extracted from a 3D, 9C wide azimuth synthetic elastic data set generated by finite-differencing. Some of the examples are noise-free and some have random noise added. The noise added to the slowness data has mean zero and variance of $\pm 2\%$ of the maximum slowness magnitude in the noise-free data. The noise added to the polarization has mean zero, and deviation of 10° randomly oriented from the noise-free polarization direction.

The modeling algorithm used in the second group of examples is the particle velocity-stress formulation of the 3D elastodynamic equations (e.g. Tessmer, 1995), implemented by eighth-order, staggered-grid, finite-differencing to solve for 3C particle velocities (Ramos-Martínez et al., 2000). The software is able to generate seismograms for anisotropic symmetries up to triclinic (with 21 independent elastic moduli). We use absorbing boundary conditions (Cerjan et al., 1985) at the top of the model to eliminate generation of free-surface multiples to facilitate clarity in understanding the results, although multiples of all types are valid for input to the inversions.

For computational efficiency, all the examples are calculated numerically by exciting three orthogonal 1C sources sequentially in the subsurface and saving the responses for each on a grid of 3C receivers on the surface which, by reciprocity for a homogeneous medium, creates the same slowness and polarization vectors as a field VSP geometry with a single 3C receiver in a borehole and 3C sources distributed on the surface. In all subsequent references to the survey geometry, we treat the data as being equivalent to a single 3C downhole receiver, and 3C sources on the surface. The same procedure can be used for simulating test data for laterally heterogeneous media.

CHRISTOFFEL EQUATION EXAMPLES

Generating test data

In this section, we generate synthetic phase slowness and polarization data vectors (Figure 2) by SVD of the classical Christoffel matrix (Appendix A) for a triclinic model (Appendix C); see for example, Helbig (1994). For the forward problem, the inputs to the Christoffel matrix (equation A-1a) are the directionally dependent elastic moduli produced by the T-matrix formulation (Jakobsen et al., 2003), from the host rock and crack properties and orientations (given in the previous section and Appendix C), along with the propagation directions for various polar and azimuth angles. For the forward problem, we use the SVD routine DSVD from LINPACK (Dongarra et al., 1979) to decompose the Christoffel matrix. Then, the eigenvectors of the SVD are the polarization vectors, and the eigenvalues are the phase velocities squared (Jech, 1981; Ditri, 1994; Carcione, 2007).

Figure 2 shows projections, onto the horizontal plane, of slowness and polarization vectors, respectively, for qP, qS1, and qS2, calculated by the Christoffel equation. The black dots in Figure 2 indicate 60 3C source positions distributed over the model surface with apertures of polar angle [15°–75°] and azimuth [0°–360°]; the 3C borehole receiver position is at $(x, y, z) = (1665, 1665, 250)$ m. The slownesses vectors for all the waves (Figure 2a, 2b, and 2c) show radial patterns. The horizontally projected polarizations for qP (Figure 2d) are approximately radial around the receiver position. The horizontally projected polarizations near the borehole for the faster S-wave (qS1) (Figure 2e) are dominated by the orientation of crack set 2 (Figure 1) which has the highest crack density (0.04).

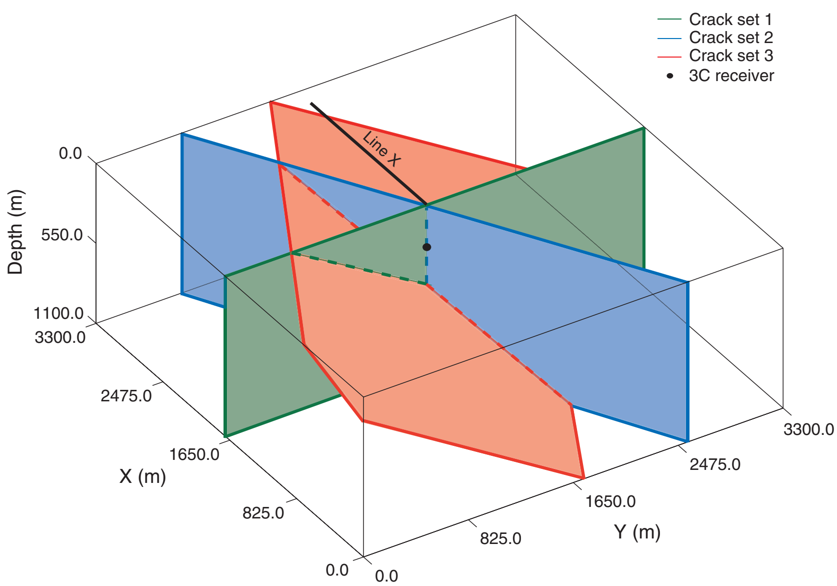

Figure 1. 3D elastic homogeneous triclinic model used to create the data for all the synthetic examples. Line X (black line) contains representative 3C source positions at depth $z = 10$ m. The solid black circle is a 3C receiver position at $(x, y, z) = (1665, 1665, 250)$ m.

The horizontally projected polarizations near the borehole for the slower S-wave (qS2) (Figure 2f) are orthogonal to those for qS1.

Inversion results for wide aperture data

In any physically realizable (isotropic or anisotropic) medium, there are general patterns in the distribution of magnitudes between groups of moduli that constrain their relative values. The "qP-wave diagonal" values c_{11}, c_{22}, and c_{33} are the largest, the "qP-wave off-diagonal" values c_{12}, c_{13}, and c_{23} are typically about half of the "qP-wave diagonal" values, the "qS-wave diagonal" values c_{44}, c_{55}, and c_{66} are typically about half the "pP-wave off-diagonal" values, and the rest are typically 10% or less of the "qS-wave diagonal" values. Particular patterns also depend on axis rotations and the anisotropy symmetry. These relations may be used to apply approximate constraints in defining appropriate starting models for inversion. The starting model for the elastic moduli, for all the inversions below, is equation C-4 in Appendix C. This is the isotropic (unfractured) host model (equation C-1) with random noise (equation C-3) added. It qualitatively satisfies the required pattern in the relative modulus values, and so is an acceptable starting model. During the inversions, no explicit constraints are applied.

Figure 3 shows the inversion results for the 21 independent elastic moduli with wide polar angle [15°–75°] and azimuth [0°–360°] apertures after six iterations with 60 data locations (Figure 3a), each with 3C polarization and 3C slowness for qP, qS1, and qS2 for noise-free and noisy data. The inversion procedure is described in Appendix B. The polar angle coverage from 15° to 75° is referred to below as the wide polar angle aperture as we consider only downgoing incident (direct) waves. If up-going (reflected) waves are included, the maximum polar aperture will be 180°. There is a good fit between the exact and inverted elastic moduli (Figure 3b). Inversion of the noise-free data (the red circles) converges in four iterations (Figure 3d). The green circles show the result from the noisy slowness and polarization components; this also converges in four iterations. In Figure 3d, the final rms residual calculated from the difference between the inverted and exact models for the noisy data is larger than that for the noise-free data by the amount of the noise.

Figure 3c and 3e shows the normalized model covariances (the correlation matrices) across all 21 elastic moduli for the noise-free and noisy data, respectively. The correlation matrix of the solution with noise is similar to that without noise as only internally consistent data contribute to the solution; random noise is not fitted and remains in the residual at all iterations (Figure 3d). The model correlation depends only on the relations between the model parameters, which are not affected by random noise (which cancels when the solution is fitted across all the data). At convergence, incoherent noise remains in the residual, so contributes to the uncertainty in the solution, but the solution itself is robust (Xu et al., 1995; Chang and McMechan, 2009). Coherent noise could distort the solution as well as the model correlation matrix.

For the noise-free and the noisy data, the dark red (high positive) covariance values on the diagonal indicate positive strong correlation of all the elements with themselves, and more importantly, independence from each other. The green and blue (low values) in the off-diagonal positions indicate weak relationships of among elements. Thus, the solution is completely and sufficiently achieved with wide polar angle [15°–75°] and azimuth [0°–360°] apertures. Note that the correlation matrix is consistent with the close fit between the estimated and the correct modulus values in Figure 3b; because the correct solution is known, we have an absolute criterion for the performance of the inversion. What is more important is that computing a correlation matrix does not require any knowledge of the correct solution, and so it provides an independent measure of parameter independence at convergence. Solutions with diagonally dominant correlation matrices are complete and reliable. We will see below that greater or lesser diagonal dominance correlates with the reliability of each parameter or group of parameters.

Inversion results for data with limited polar angle aperture

Figure 4b shows the inversion results for the noisy data distributed with azimuths of [0°–360°], and fixed polar angles of 15° (red) or 75° (green) (Figure 4a). These are extreme examples, designed to illustrate particular characteristics of the correlation matrices; they are not recommended field geometries. The results show that both solutions are incomplete and insufficient as indicated by elements that converge to local minimum values away from the correct solution (Figure 4b). The inversion procedure converges in three iterations (for polar angle of 15°) and four (for polar angle of 75°),

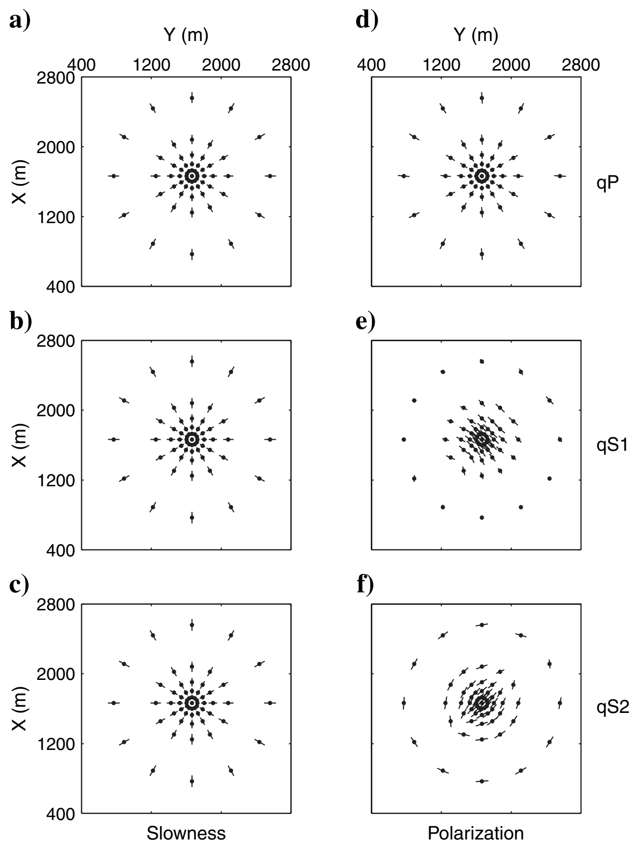

Figure 2. Horizontally-projected slowness and polarization vectors, are in the left and right columns, respectively, for qP (a and d), for qS1 (b and e), and for qS2 (c and f) calculated by the Christoffel equation. The black dots indicate 3-C source positions distributed with apertures of polar angle [15°–75°] and azimuth [0°–360°] at $z = 10$ m, and the circular dot in the center of each plot is a 3-C receiver position at $(x, y, z) = (1665, 1665, 250)$ m.

indicated by flattened rms residuals (Figure 4d) which are much larger than the final residuals of the previous example with noise added. Figure 4d shows rms residuals ~7.90 km^2/s^2 and ~1.89 km^2/s^2 for polar angles of 15° and 75°, respectively. The final rms residuals are mostly associated with c_{11}, c_{22}, and c_{66} for polar angle of 15°, and c_{33} for polar angle of 75° (Figure 4b).

In Figure 4c, the model correlations for the solution for the data propagating at the (near-vertical) polar angle of 15° (but over all azimuths) shows that only the moduli c_{33}, c_{34}, c_{36}, c_{44}, c_{55}, c_{56}, and c_{66} are solvable, but of these only c_{34}, c_{56}, and c_{66} are relatively independent. For example, the near-vertical P-wave velocity $c_{33}^{1/2}$ is solvable, but is correlated with c_{11} through c_{16}, and with c_{22} through c_{26}. Similarly, in Figure 4e, the model correlations for the solution for the data propagating at the (near horizontal) polar angle of 75°, show that the moduli c_{11}, c_{22}, and c_{66} are solvable, but are not independent; they interact strongly with many other moduli, as indicated by the vertical and horizontal lines through these points. For example, c_{11} interacts only with c_{12}, but c_{66} interacts with all the other moduli. This contamination is caused by interdependence of estimated moduli associated with insufficient constraints; the result is that their values are apparent, not exact. Poorly constrained parameters are not independent of each other. This is the classic trade-off between resolution and variance (e.g., Jackson, 1972; Menke, 1989).

Inversion results for data with limited azimuth aperture

Figure 5b shows the inversion results for the noisy data distributed with polar angles of [15°–75°], and azimuth apertures of either [0°–90°] (green) or [90°–180°] (red) (Figure 5a); both solutions are close to the correct model; that for the [90°–180°] data is slightly better than that for [0°–90°]. Figure 5d shows that both inversion procedures converge with rms residuals ~0.21 km^2/s^2, which is consistent with the noise level contained in the data (compare with Figure 3d). Figure 5c and 5e show the model correlations across all 21 elastic moduli with azimuths of [0°–90°] and [90°–180°], respectively. The correlation matrices show high correlations along the diagonals (dark red), showing that reliable solutions can be obtained with these survey geometries. Comparing Figure 5c and 5e with the model correlations of the wider azimuth aperture data (Figure 3c and 3e), we see substantially larger off-diagonal values here, and they are biased toward either negative (Figure 5c) or positive (Figure 5e) values as the

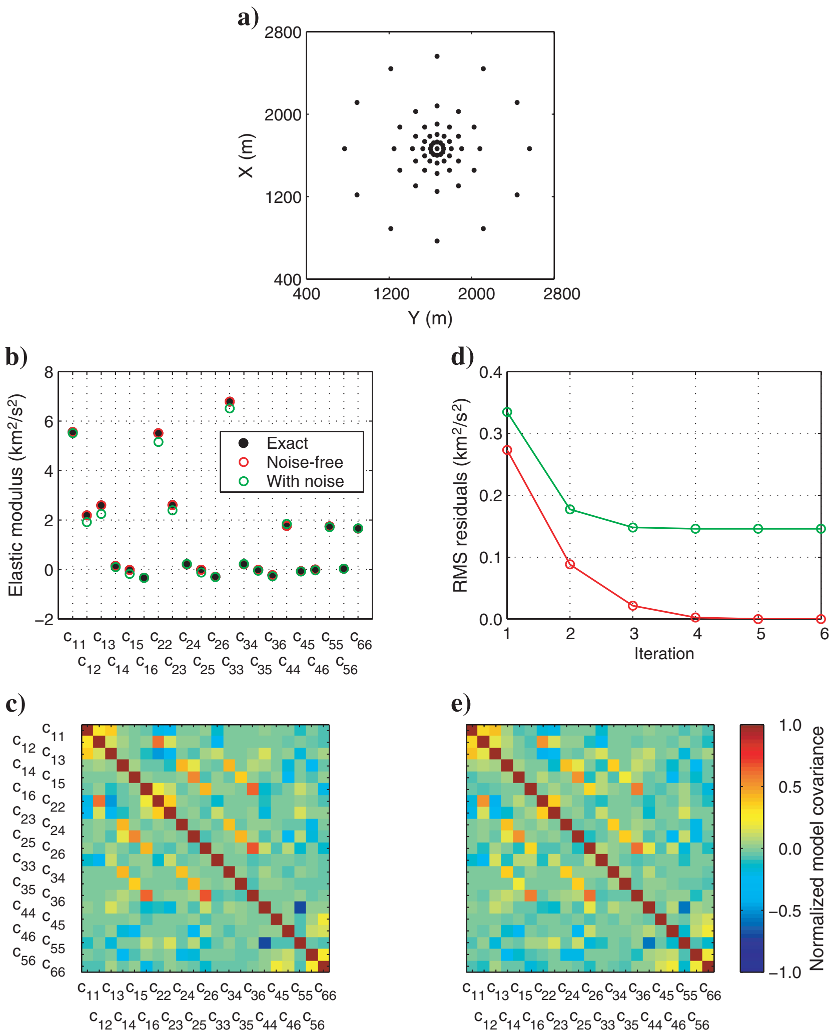

Figure 3. (a) a receiver position (the circular dot in the center of the plot) and 60 surrounding source locations to give wide apertures of polar angle (15°–75°) and azimuth (0°–360°) in the data used as inputs to inversion. (b) the inversion results for 21 elastic tensor elements, for noise-free and noisy data, after six iterations. (d) the corresponding rms residual distributions over six iterations. (c) and (e) the model correlations across all 21 elastic moduli for the noise-free and noisy data, respectively.

corresponding data are directionally-biased samples (Figure 5a). As the amount of information in the data decreases, through polar angle or azimuth aperture decreases, the interparameter dependence increases as the solution attempts to fit across all the parameters; that is, less data lead to less unique solutions (less diagonal dominance) and less parameter independence (higher off-diagonal values). The off-diagonal value clusters in Figure 5c and 5e correspond to interactions between different groups of moduli, as a consequence of the different sampling of the moduli by waves propagating at different azimuths. The parameter interactions shift in correlation space as the azimuth window changes. Note that, although the parameter correlations do not directly depend on the data, the model at convergence does depend on the sampling of the model by the data.

Convergence behavior for limited polar and azimuth angle apertures

Figure 6 shows the composite rms residuals across all 21 elastic moduli as a function of either the polar angle (open circles) or the azimuth (closed circles) aperture, while keeping the other aperture at its widest extent, both for the noisy data. The residuals are obtained by taking the rms of the difference between the inverted and correct moduli; rms residuals decrease as the polar angle or azimuth aperture increases. The largest residuals ($>7.90\ \mathrm{km^2/s^2}$) are for inversions using data apertures of polar angle of 15° and azimuth of [0°–360°], or polar angles of [15°–75°] and azimuth of 0°; these apertures are not enough to constrain the solution as they do not adequately sample the elastic moduli. The smallest residuals ($<0.21\ \mathrm{km^2/s^2}$) result from the inversions using the data apertures of polar angle of >45° and azimuth of [0°–360°], or polar angles of [15°–75°] and azimuth aperture of >90°; these apertures are sufficient to constrain the solution. Use of the full polar angle and azimuth apertures are strongly recommended for estimating all 21 elastic moduli. A full polar angle aperture with partial azimuth aperture is preferred over a full azimuth aperture and only a small polar angle aperture; for this example. For field VSP data, the polar angle aperture may be relatively full as direct and reflected (downgoing and upgoing) waves are both present, and direct waves with incident angles near, and beyond, 90° are produced by turning in a positive velocity gradient.

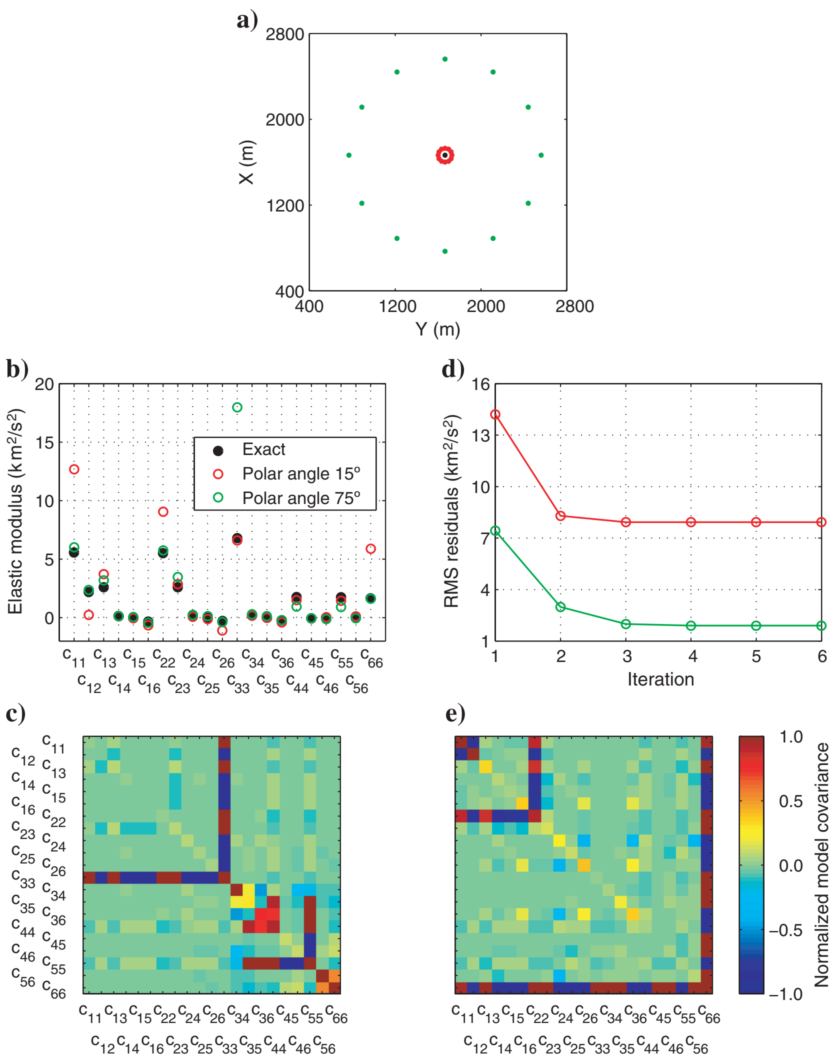

Figure 4. (b) Inversions for 21 elastic moduli using the noisy data distributed with azimuths of [0°–360°], and fixed polar angle of 15° (red circles) or 75° (green circles) in (a). (d) The corresponding rms residual distributions over six iterations. (c) and (e) The model correlations across all 21 elastic moduli obtained by inversion of data with polar angles of 15° and 75°, respectively.

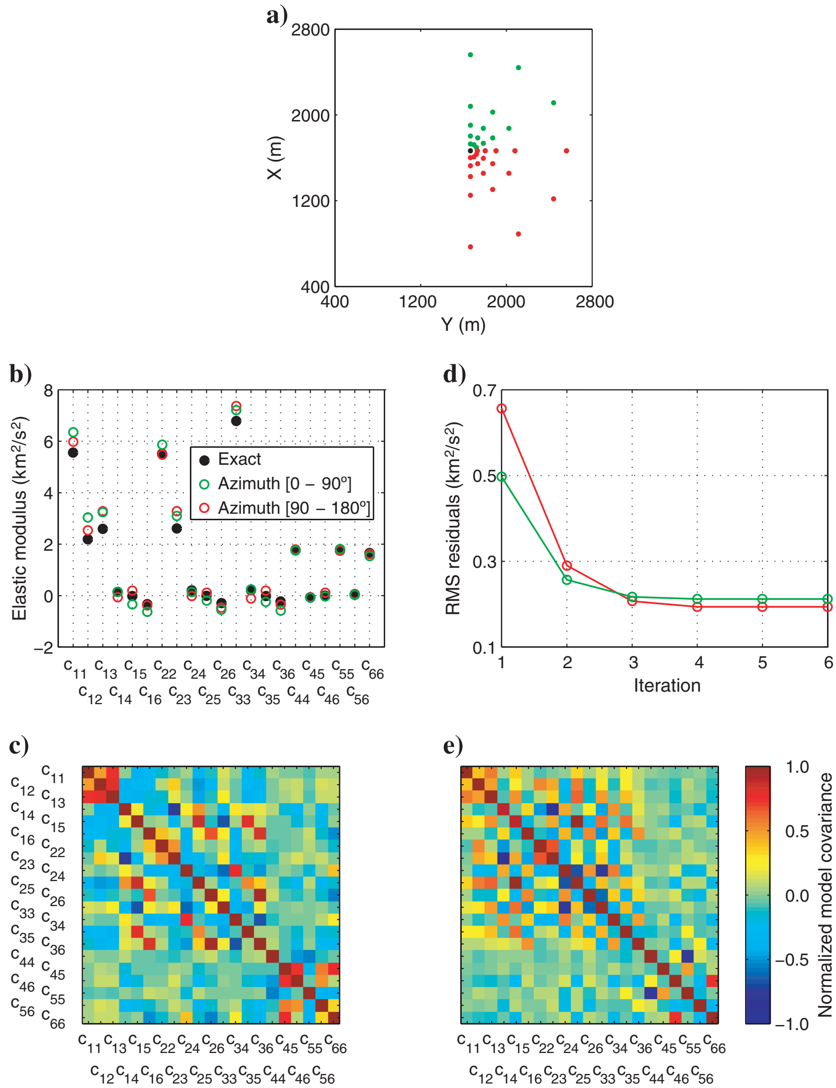

Figure 5. (b) Inversions for 21 elastic moduli using the noisy data distributed in (a) with polar angles of [15°–75°], and azimuth apertures of [0°–90°] (green circles) or [90°–180°] (red circles). (d) The corresponding rms residual distributions over six iterations. (c) and (e) The model parameter correlation matrices across all 21 elastic moduli with azimuths of [0°–90°] and [90°–180°], respectively.

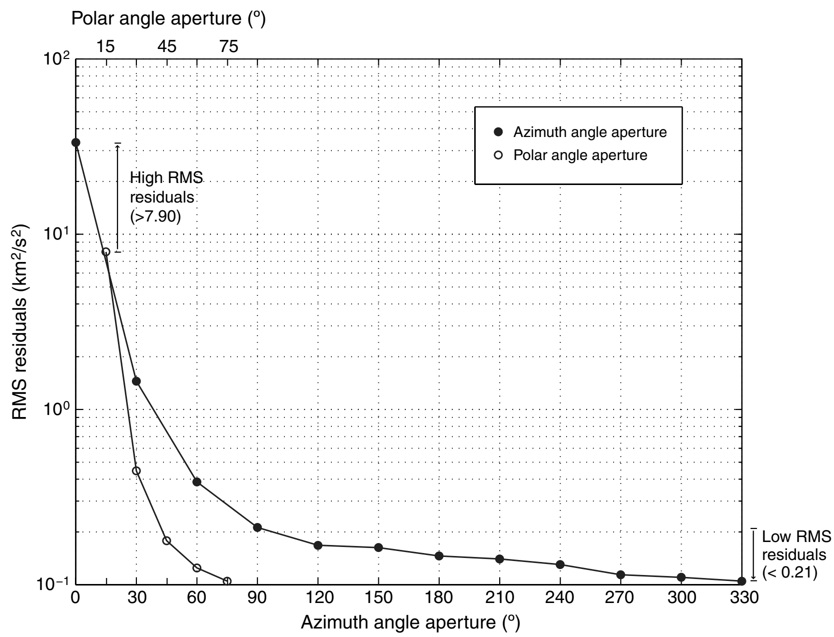

Figure 6. The rms residuals calculated from the difference between the inverted and exact models across all 21 elastic moduli as a function of polar angle (open circles) and azimuth (filled circles) apertures, both for the noisy data. As we consider only downgoing waves, the maximum possible polar angle aperture is 90°.

Solutions without horizontal components of slowness data

One of the limitations of the examples above is that they all include the horizontal components of the slownesses (calculated analytically via the Christoffel equation). This implicitly assumes that these are approximated by computing time derivatives on the surface, which in turn will be accurate only if the material above the geophone is homogeneous or nearly so (Bona and Slawinski, 2008). This restriction is a consequence of the necessity to be able to tie the horizontal slowness components measured at the surface to those that would be measured in the subsurface; as the slowness depends on the incident direction, this tie is unique only if the propagation path is straight, or if the velocity model is known in detail. Thus, it is important to consider solutions that do not require horizontal slowness components as input. One approach is that of Dewangan and Grechka (2003) who move the horizontal slownesses from the data vector of the linear system, to the unknown vector, and solve for them along with the moduli; this makes the inversion nonlinear. A second approach is the linearlized formulation given by Gomes et al. (2004) who also remove horizontal slownesses from both the data parameterization, by using the interdependence of the horizontal slowness components and the polarization (Zheng and Pšenčík, 2002).

For the next example, we use the formulation of Dewangan and Grechka (2003) (their Scenario 3), which assumes 3-C geophones in a vertical borehole, so vertical slownesses and 3-C polarization can be extracted from qP, qS1, and qS2 data, but no horizontal slowness components. The latter removes all assumptions of homogeneity above the geophone. The input data are the vertical slownesses and 3-C polarizations for qP, qS1, and qS2 waves for all 60 sources in the wide aperture geometry in Figure 3a. The solution is for the six missing horizontal phase slownesses along with the 21 elastic moduli.

The solutions for noise-free and noisy data are in Figure 7. The results are very similar to those in Figure 3 (which correspond to Dewangan and Grechka's Scenario 1); the residuals (Figure 7c) are a little higher, as are the off-diagonal correlations (Figure 7b and 7d). The two noise-free solutions, with and without the horizontal slownesses (Figures 3b and 7a) are virtually identical and the two noisy solutions have similar, small residuals. The correlation matrices (Figure 7b and 7d) show that all 21 moduli are recovered and are fairly independent of each other. A difference is that the solutions without horizontal slownesses take longer to converge (from the same starting model); nine iterations versus five. The main cause of this difference is probably the fact that, when horizontal slowness components are not included in the input data, that the solution becomes underdetermined because of the larger number of unknowns (Dewangan and Grechka, 2003); this accounts for the slower convergence and the larger final residuals for some of the moduli for the noisy data.

The main practical observation is that, while the horizontal components of the slowness vector are (at least implicitly) required for the computation of the 21 elastic moduli, when polarizations are used, it is not necessary to observe the horizontal slowness components. This is important as it means that all the required data for a complete solution can be obtained from 3C borehole measurements; horizontal slowness components do not have to be estimated at the surface (although this is still a viable way to get starting values of horizontal slownesses for the inversion).

Inversion results using qP waves only and qS waves only

The examples above illustrate the results of varying the polar and azimuth angle apertures when 3C slownesses and 3C polarizations for qP and qS waves are present, or with or without the horizontal slownesses. Now consider inversion of the wide aperture data

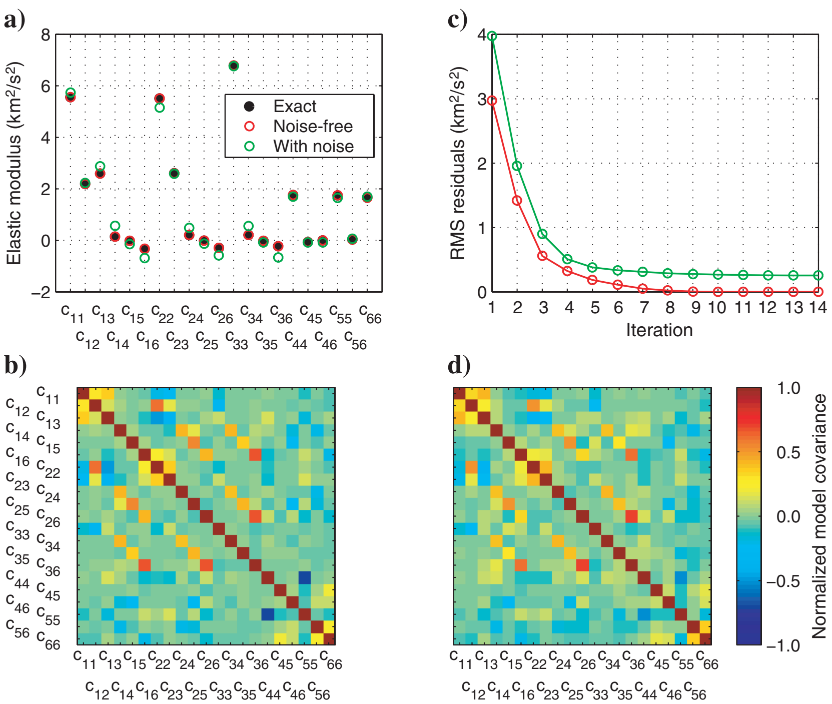

Figure 7. (a) Inversion results for noise-free and noisy input that do not include horizontal slownesses, after 14 iterations. (c) The corresponding rms residuals as a funtion of iteration number. (b) and (d) The model parameter correlation matrices across all 21 elastic moduli for the noise-free and noisy data, respectively.

(Figure 3a) when only the qP-wave data, or only the qS-wave data, is available.

For the qP-wave inversion, in this example, three noise-free components of qP-wave slowness and polarization are input, for each of the 60 sources, and inverted for the 21 elastic moduli. For the qS waves, there are two wave types, qS1 and qS2, so there are six components of slowness and six components of polarization, per source location; for qS waves, there are twice as many input data as for the qP waves. The data are generated using the Christoffel equation; the inversions use the algorithm in Appendix B to facilitate comparison with the results in Figure 3.

The inversion results for the 21 moduli are shown in Figure 8 for the separate qP- and qS-wave inversions. The residuals at convergence (Figure 8c) for the qS-wave data are about half of those for the qP-wave data, as there are two qS waves and only one qP wave. Even though there is no noise added to the data, the residuals are significantly higher than those for inversion of the combined qP- and qS-wave data in Figure 3c. The individual solutions (Figure 8a) are also worse than that for the combined data in Figure 3b, with the qP residuals being smaller for the moduli that mainly influence the qP propagation (in the left half of Figure 8a) and the qS residuals being smaller for the moduli that mainly influence the qS propagation (in the right half of Figure 8a). The model correlations for the qP and qS solutions (Figure 8b and 8d, respectively) show the same information in a different, more detailed, form. The correlation patterns for the qP and qS solutions are complementary; where one is high, the other is low, and vice versa because of the orthogonality of the qP and qS polarizations. This complementarity is also seen in Figure 4c and 4e where the solutions are for nearly orthogonal propagation directions. The qS-wave solution gives reliable moduli for c_{34} through c_{66} (Figure 8d). (Compare with Figure 3d and 3e).

FINITE-DIFFERENCE EXAMPLES

Generating test data

The examples above use data generated analytically from the Christoffel equation, and so are fairly complete and accurate. In this section we measure the phase slowness and polarization components from 9C synthetic seismograms generated to simulate a VSP experiment for a triclinic model (equation C-2) and invert for the 21 elastic moduli from these data. This finite-difference example illustrates procedures needed for field data, and allows a specific evaluation of how well the inverted moduli can account for the seismic observations. The modeling algorithm is a particle velocity-stress formulation implemented by eighth-order, staggered-grid, finite-differencing (Ramos-Martínez et al., 2000). The dimensions of the model in the x-, y-, and z-directions are $331 \times 331 \times 111$ grid points with 10 m spacing ($3300 \times 3300 \times 1100$) (Figure 1). The dominant frequency of the Gaussian source wavelet is 26 Hz. For creating the synthetic test data, all six model boundaries are set to absorbing by using the tapering algorithm of Cerjan et al. (1985), with tapering zone widths of 60, 20, 40 grid points at the top, bottom, and vertical sides, respectively. The time sample increment is 0.85 ms, and the total record length is 2.125 s. The 3C receiver is located at $(x, y, z) = (1665, 1665, 250)$ m and the 3C sources are distributed over the top of the model in a 331×331 array at depth $z = 10$ m. The data used for the inversions span apertures of polar angle [15°–75°] with 15° increment and azimuth [0°–360°] with 30° increment.

Figure 9 shows representative direct arrivals in the unrotated 9C VSP data, simulated for recording along the Line X (the black line parallel to the x-axis in Figure 1). In Figure 9, the first letter at the upper right corner of each panel corresponds to the source orientation, and the second corresponds to the receiver orientation. For

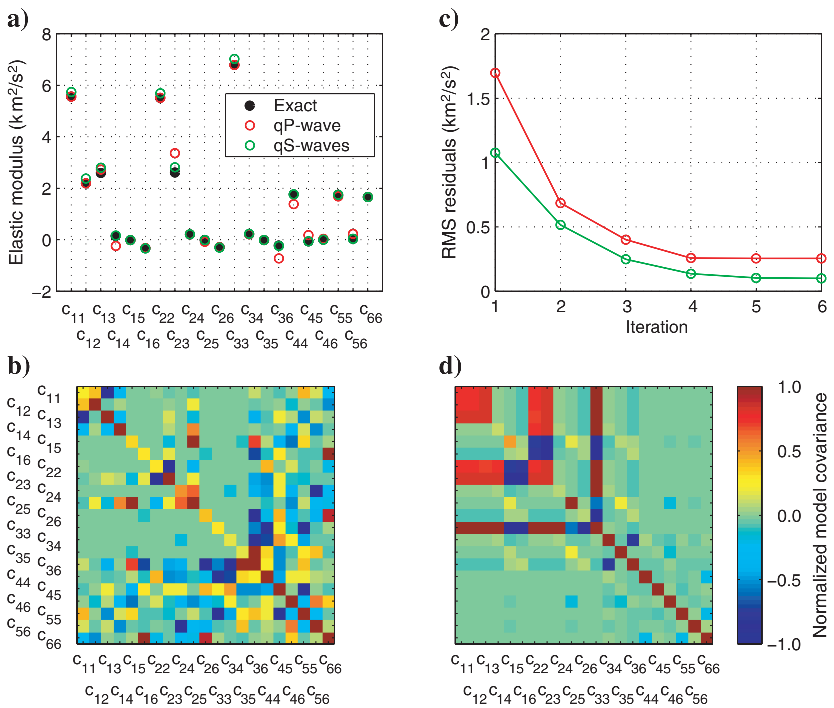

Figure 8. (a) Inversions for 21 elastic moduli obtained using only noise-free qP (red circles) and qS (green circles) data computed by the Christoffel equation, and distributed over the wide slowness and polarization angle apertures (Figure 3a). (c) The corresponding convergence behavior for six iterations. (b) and (d) The model parameter correlation matrices across all 21 elastic moduli from qP- and and qS-wave data, respectively.

example, XY means that the data are generated from the horizontal force component of the source oriented parallel to the x-axis, and recorded on the horizontal receiver component oriented parallel to the y-axis (Figure 1). Figure 9 is one slice through the 9C data volumes. For the subsequent inversion, the data distribution in Figure 10 is used.

The seismogram sections in Figure 9 are complicated because of the triclinic structure and the raw data are not rotated into their principle components (Adam, 2003). Responses at other azimuths show energy partitions, across the nine components that are different from those along the Line X because of the relative rotation between the wavefronts in the data and the geophone orientations.

For this example, horizontal and vertical components of the phase slownesses are obtained by taking the first derivatives of traveltimes with respect to the source and receiver positions, respectively (e.g., Gaiser, 1990), assuming homogeneity of the overburden. The receiver is located at 250 m depth. Three-component polarizations of qP and qS waves are calculated by SVD, as described in the "Phase slowness and polarization data" subsection. The inputs to inversion are nine components of slowness and nine components of polarization (three of each, for each incident qP, qS1, and qS2 wave). After inversion (Appendix B), the 21 inverted elastic moduli are input to full wavefield finite-difference modeling and the resulting predicted seismograms are compared with the input "observed" seismograms. A final example uses Dewangan and Grechka's (2003) Scenario 3, which solves for, rather than inputting the horizontal slownesses.

Figure 10 shows projections, onto the horizontal plane, of three sets of polarization vectors; those measured from the synthetic data (in the left column), calculated by the Christoffel equation from the inverted elastic moduli with horizontal slownesses in the input data (in the center column), and calculated by the Christoffel equation from the inverted elastic moduli without horizontal slownesses in the input data (in the right column), for qP, qS1, and qS2 waves. Comparing with the polarizations for the correct solution in Figure 2d, 2e, and 2f shows only small differences between them. The difference may be caused by errors in calculating the polarizations from the data, which propagate as an uncertainty into the inverted elastic moduli. The corresponding slowness vector components are not shown; they are essentially identical to each other and look like those in Figure 2a, 2b, and 2c. The measured polarizations in Figure 10a, 10b, and 10c, along with the corresponding 3C slownesses, are input to the inversion, whose results are in Figure 11a, 11b, and 11c. The corresponding results, when only vertical slownesses are input, are in Figure 11d, 11e, and 11f.

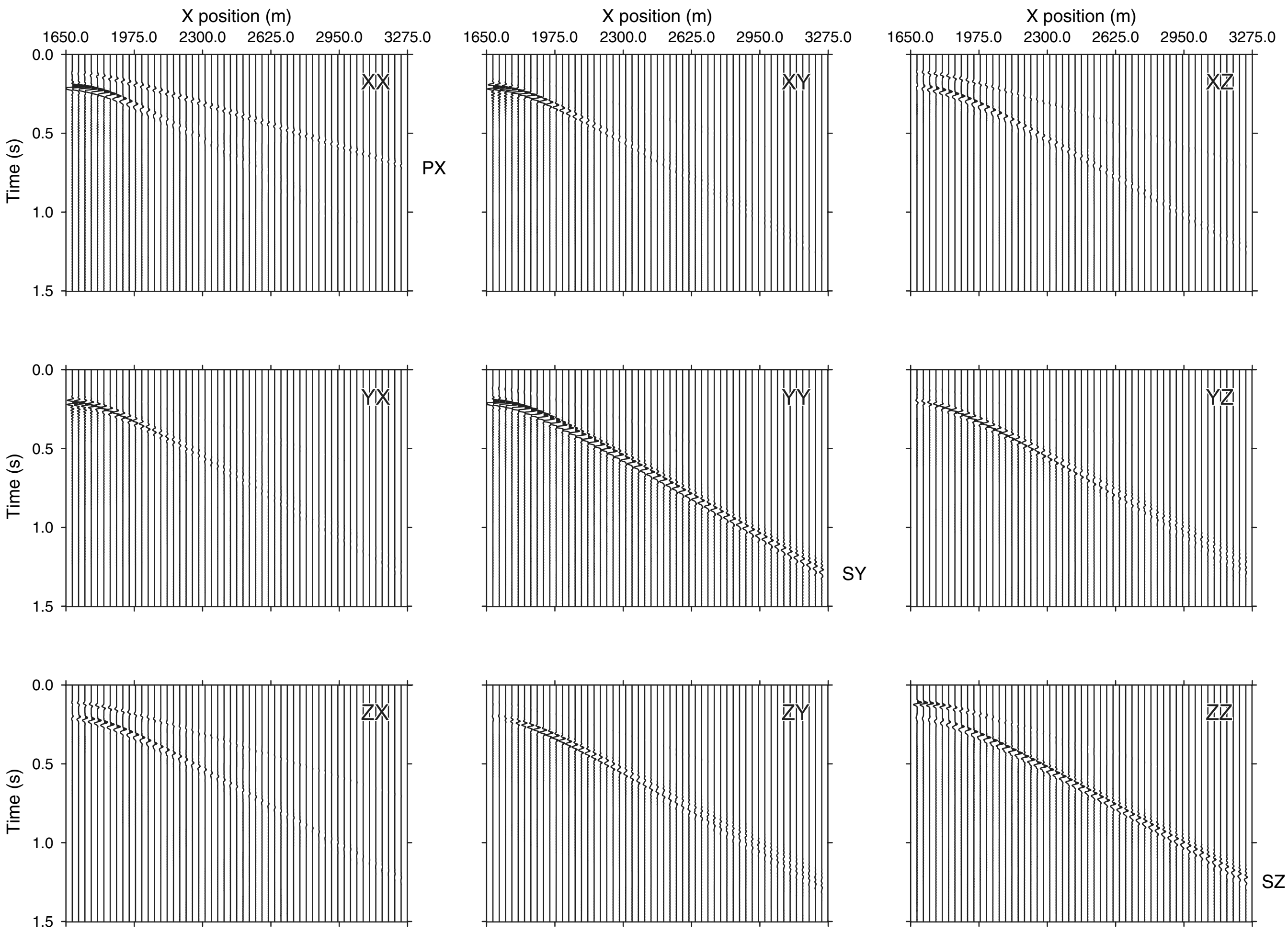

Figure 9. Representative raw (unrotated) 3D, 9C synthetic VSP data, recorded on a 3C receiver at $(x, y, z) = (1665, 1665, 250)$ m, for 3C sources along the Line X (above the receiver, parallel to the x-axis) in Figure 1. Some of the main downgoing waves are labelled.

Inversion results

Two configurations are presented; the left column of Figure 11 shows the results when the input data include horizontal slowness components estimated at the earth's surface, and the right column has the results when they are not. The polarization and slowness components that are input to the inversion are measured from the synthetic seismograms, and so have measurement uncertainties in them. Figure 11a shows the inversion results for the 21 elastic moduli for the noise-free synthetic data generated for wide polar angle and azimuth apertures. Figure 11b shows corresponding rms residual over six iterations. The inverted model (Figure 11a and equation C-5) fits well with the exact model (equation C-2). The inversion converged in four iterations, with rms residuals of the density-normalized elastic moduli of $\sim 0.11\ \mathrm{km}^2/\mathrm{s}^2$ (Figure 11b). The residuals in the inverted model are caused by numerical noise in the data, and uncertainties in calculating the polarizations and phase slowness components from the data. These errors propagate as uncertainties into the inverted elastic moduli. The dark red (high positive) covariance values near the diagonal (Figure 11c) indicate strong positive correlation of all the elements with themselves; the solution is well constrained by the wide polar angle [15°–75°] and azimuth [0°–360°] apertures of the finite-difference data.

Figure 11d, 11e, and 11f contains the inversion results for the same data as that used in Figure 11a, 11b, and 11c, except that the horizontal slownesses are solved for (via Dewangan and Grechka's (2003) Scenario 3 approach), rather than being input. The results, especially the diagonal dominance of the correlation matrix, are essentially the same as those when the horizontal slowness components were also input. As in Figures 3 and 7, the omission of horizontal slowness results in slightly larger residuals at convergence, and takes more iterations to converge (eight versus four), but not having to approximate the horizontal slownesses is an overriding advantage for field data.

Results of inversion of 3C slownesses and 3C polarizations of qP data alone are in the left column of Figure 12 and for inversion of the qS1 and qS2 waves alone are in the right column. The results again are very similar to those using the same inversion procedure in Figure 8, which used noise-free data calculated by the Christoffel equation. The general patterns in the correlation matrices in Figures 8 and 12 are similar, and the qP and qS correlation distributions are complementary because of the orthogonality of the qP and qS polarizations.

To close the loop, the left column of Figure 13 shows the synthetic seismograms calculated from the elastic moduli obtained by inversion without horizontal slowness components in the input (Figure 11d); the right column shows their residuals from the corresponding input seismograms in Figure 9. Only the representative components XX, YY, and ZZ recorded on Line X (Figure 1) are shown. The residuals approach zero for qP in all three components. Small residuals remain for qS in YY, and are associated with small time and amplitude differences in the predicted seismograms that are a consequence of imperfect recovery of some of the small moduli, such as c_{14}, c_{24}, and c_{34} (Figure 11d).

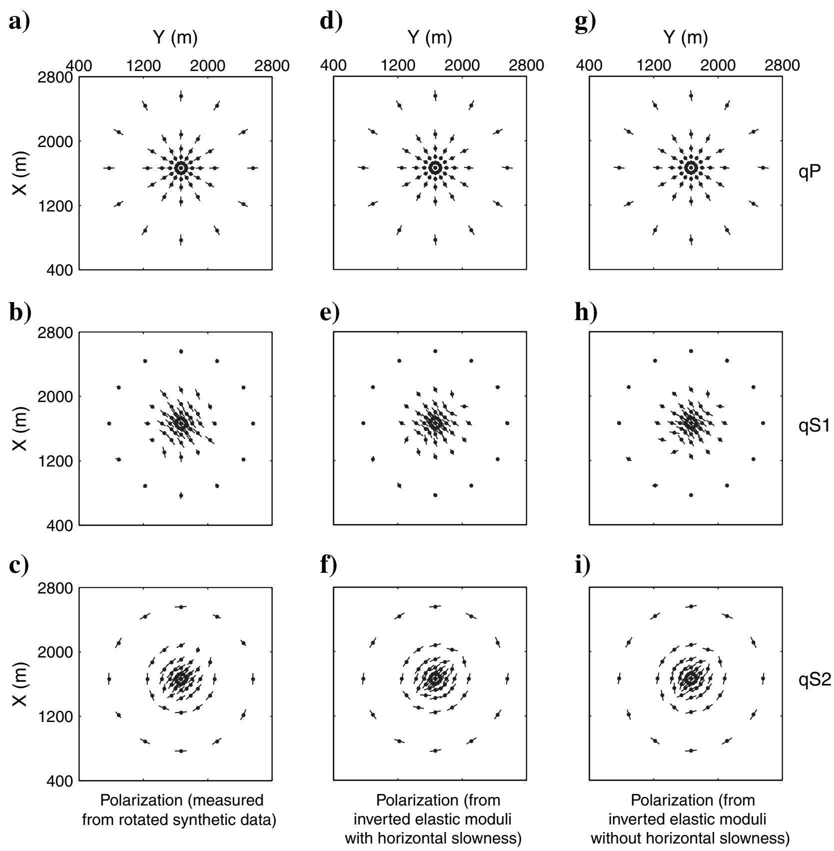

Figure 10. Horizontally-projected polarization vectors measured from the synthetic data (the left column), calculated by the Christoffel equation from the elastic moduli inverted from the noise-free synthetic data volumes with horizontal slownesses (the center column) and without (the right column). The upper, middle, and lower rows are for qP, qS1, and qS2. Compare with the correct values in Figure 2. The corresponding slowness components are not shown; they are visually indistiguishable from each other and look like those in Figure 2a, 2b, and 2c.

Figure 14 shows normalized rms residuals (circles) calculated from the difference between each of the 9C synthetic seismogram volumes calculated from the inverted elastic moduli (when horizontal slownesses are not in the input data) and the corresponding the input data volumes. The value used for normalization of all nine input data volumes is the maximum across all nine volumes. Each rms residual represents the misfit for its respective volume. The horizontal dashed line shows the maximum-value-normalized rms residual (0.0036) over all the 9C synthetic seismogram volumes. The corresponding value for the solution in Figure 11a (with horizontal slownesses) is 0.0035, so there is no significant difference between the data fits of these two models.

DISCUSSION

For field data, for a given incident angle for any wave type, the vertical components of phase slowness and all the polarization measurements are local to the downhole receivers, and therefore relatively independent of the complexity of the overburden (e.g., Dewangan and Grechka, 2003; Nistala and McMechan, 2005). For field data, we also need to determine the 3C geophone orientation (e.g., DiSiena et al., 1984; Zeng and McMechan, 2006), and to ensure vector fidelity for the polarization data (e.g., Gaiser, 2003, 2007; Burch et al., 2005). In the current project, the correct solution is known, so we have an absolute criterion for the correctness of the inversion solutions; this is not the case for field data.

Although quite complete information is potentially obtained, the cost of acquiring 3D, 9C seismic/VSP data remains a disadvantage that restricts its practical use compared to 3C and 1C data (Kendall and Davis, 1996). Thus, the potential for obtaining anisotropic solutions from reduced data sets (Jech, 1991; Gomes, et al., 2004) is attractive. Rusmanugroho and McMechan (2010) note some symmetries of 3D, 9C seismic data which potentially reduce the acquisition cost in simple anisotropies.

The polar angle illumination aperture can be increased by including upcoming (reflected) waves as well as the downgoing (direct) waves in the polarization and slowness measurements (e.g., Gomes et al., 2004). However, the direct waves provide the strongest amplitudes and are easier to use than the reflected waves as these

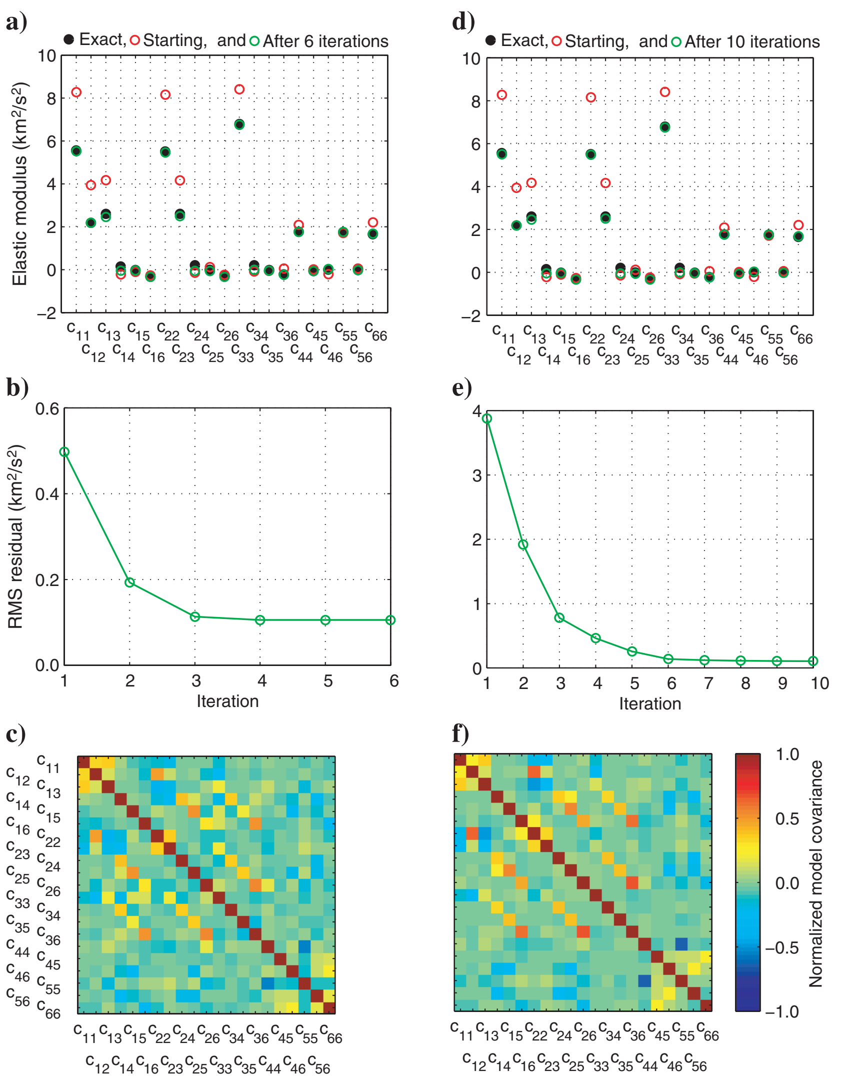

Figure 11. Inversion results for the noise-free synthetic data in Figure 8 with horizontal slowness components (in the left column), and without (in the right column). The data are for the wide angle apertures of slownesses and polarizations (Figure 3a). (a and d) The output of the inversions; (b and e) The residuals as a function of iteration number; (c and f) The model parameter correlation matrices, respectively.

are first arrivals. Including reflected waves adds more observations, and hence more constraints to the solution. The use of 9C VSP data gives an advantage as strong qP and qS waves are directly generated by surface sources. In the conventional seismic using an explosive source with a single or 3C receiver, qS waves are often obtained as converted qP-qS waves, but these are limited in their radiation patterns. Hardage et al. (2003) note that particular polarizations in 9C data characterize some anisotropic parameters better than 3C data do. Specifically, the apertures in which usable polarization and slowness information is present, are increased by using 9C data. While 3C data are theoretically sufficient to invert for the 21 elastic moduli, the polarization and slowness spaces are more reliably sampled by the broader range of amplitudes contained in 9C data. A key practical application is comprehensive characterization of a fractured reservoir in the vicinity of a borehole by inversion for the complete set of elastic moduli. Although it is beyond the scope of the present paper, this is the initial step in recovering anisotropic symmetry (Kochetov and Slawinski, 2009), fracture orientation, fracture density, and the properties of fracture-filling fluids for use in defining production strategy, time-lapse fluid replacement monitoring, and hydrofracture evaluation. For example, Davis et al. (2003) examine qP- and qS-wave reflected amplitudes from time-lapse (4D), 9C surface seismic data for monitoring CO_2 injection. The next step is application to VSP field data.

Although we have constructed examples for a number of configurations of interest, much more can be done in future research. One example is to use only one component (e.g., vertical) sources; a source with a single force component reduces the reliable (usable incident angle) ranges of slowness and polarizations, but also reduces the acquisition cost. It should be noted that some of the examples above are given only for data generated with the Christoffel equation, or only for the finite-difference data, but both use the same recording geometry, so the results are generalizable from one to the other. More detailed studies can be made of the responses of specific anisotropic symmetries and their orientations to specific survey geometries (Helbig, 1994) and vertical changes in anisotropy can be defined with data from geophones at a sequence of depths in the borehole (Adam, 2003).

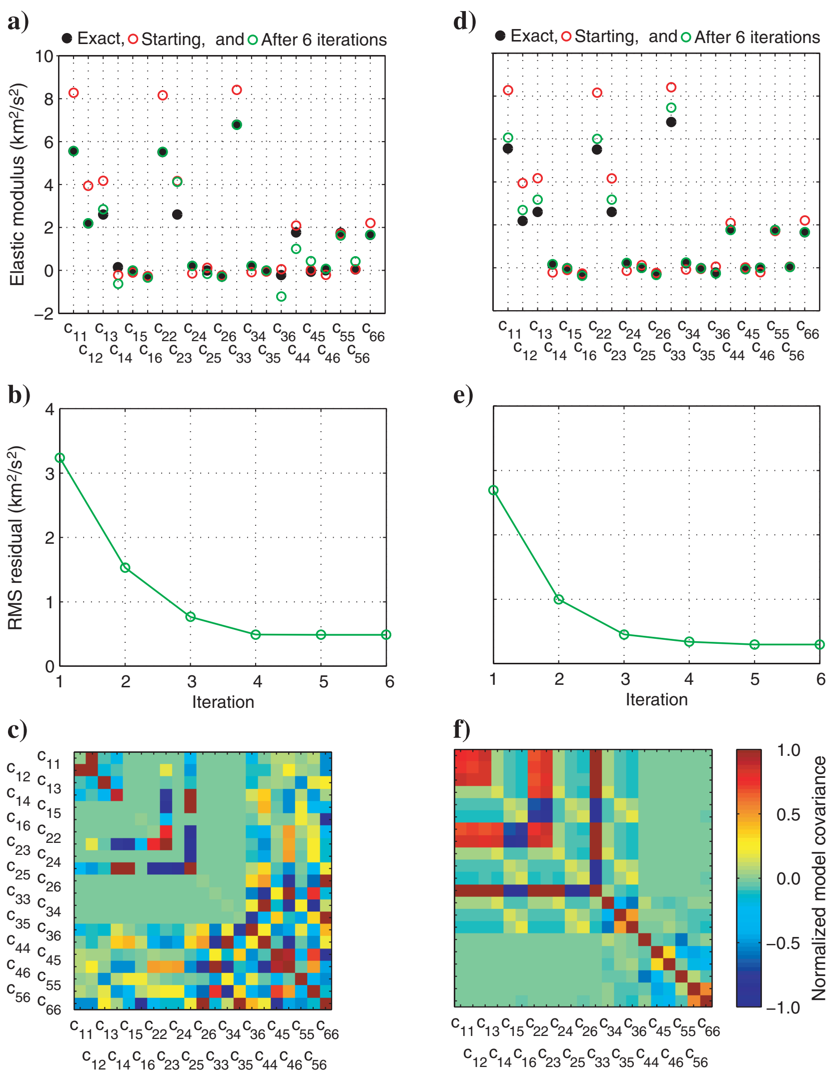

Figure 12. (a and d) The inversion results for the synthetic qP- and qS-wave (qS1 and qS2) data, respectively, with horizontal slownesses, both with the wide apertures of polar and azimuth angles as in Figure 3a. (b and e) The corresponding rms residual distributions over six iterations. (c and f) The corresponding model parameter correlation matrices.

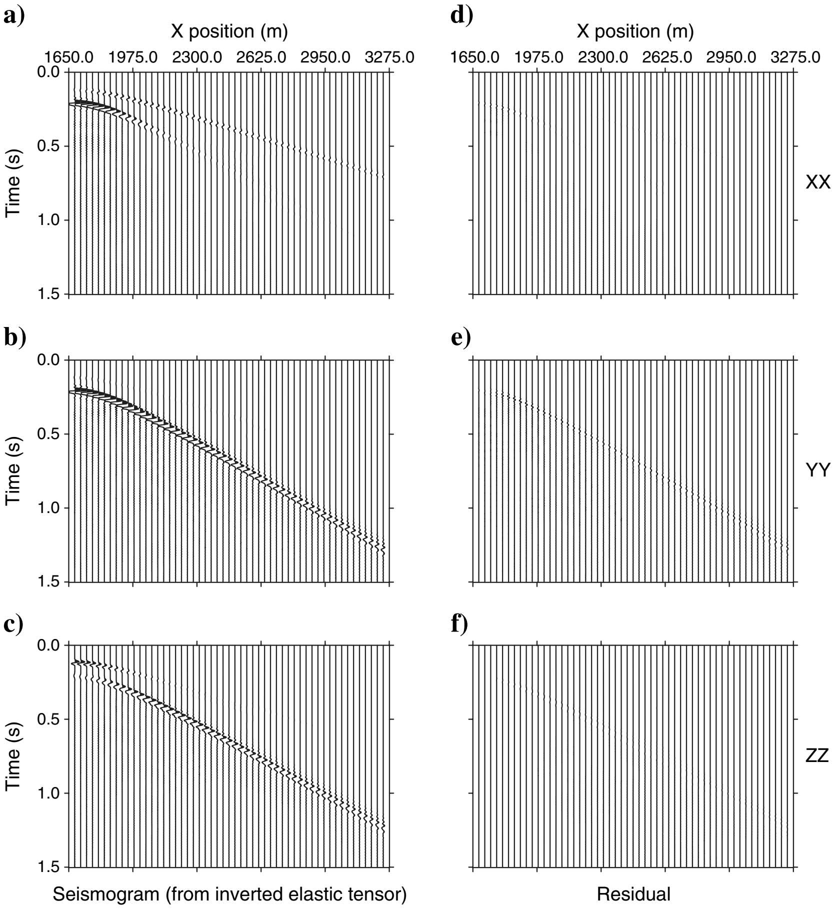

Figure 13. Synthetic seismograms (a, b, and c) created using the inverted elastic moduli, for the model in Figure 11d and their residuals (d, e, and f) relative to the corresponding seismograms in Figure 9, in the left and right columns, respectively. Components are XX (a and d), YY (b and e), and ZZ (c and f).

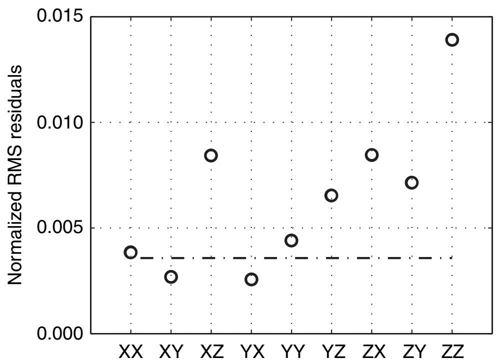

Figure 14. Normalized rms residuals (circles) calculated from the difference between each of the 9C synthetic seismogram volumes computed from the inverted elastic tensor elements, and the corresponding 9C input seismogram volume. Normalization is to the maximum value over all of the 9C input component data volumes. The seismogram data differences for one representative slice through three of the 9C volumes are shown in Figure 13. The dashed line shows the maximum value-normalized rms residual, from the input data, over all the 9C synthetic seismogram volumes.

CONCLUSIONS

The quality and completeness of the inversion of slowness and polarization data for the 21 elastic moduli in the neighborhood of a 3C borehole geophone depend on the number and angular apertures of the observations, the noise level, wave types, the apertures of the polar and azimuth angles and the parameterization and algorithm chosen for inversion. Solutions using synthetic slowness and polarization components calculated directly from the Christoffel equation illustrate the procedures and tradeoffs. Nine-component elastic synthetic seismograms for a model with triclinic symmetry calculated by finite-differencing in a VSP geometry illustrate estimation of the elastic moduli. All the required data for inversion of all 21 elastic moduli are potentially available from downhole 3C geophones. The moduli become less independent as the sampling of the anisotropic moduli by the data geometry decreases. Horizontal slownesses are not required to be input, with the acceptable trade-off of slower convergence of the solution caused by having fewer data, not less independent information. The qP and qS waves in any given incident direction constrain the estimation of different elastic moduli as they have orthogonal polarizations; similarly, windows in azimuth and/or polar illumination angles correspond to selective sampling of the modulus solution space.

Calculation and use of correlation matrices is valuable in interpretation of solutions. For any particular data subset, they reveal which moduli are solved as independent parameters, which are correlated, and which are unsolveable for lack of relevant constraints in the data.

ACKNOWLEDGMENTS

The research leading to this paper was supported by the Sponsors of the UT-Dallas Geophysical Consortium. We use the double precision routine dsvd from the LINPACK library to decompose the Christoffel matrix, and routine lmdif from the MINPACK library to perform the inversions in the examples. Constructive comments by I. Pšenčík, S. Leaney, and an anonymous reviewer are appreciated. This paper is Contribution No. 1221 from the Geosciences Department at the University of Texas at Dallas.

APPENDIX A

THE CHRISTOFFEL EQUATION

The classical definition of the 3×3 Christoffel matrix is

$$\Gamma_{ik} = C_{ijkl} n_j n_l, \tag{A-1a}$$

where C_{ijkl} contains the stiffness elements of the modulus tensor and n_j and n_l are components of a unit vector that specifies the normal to the wavefront of a considered wave (e.g., Helbig, 1994). The Christoffel equation corresponding to matrix A-1a is

$$[\Gamma_{ik} - \rho(v^{(Q)})^2 \delta_{ik}] A_k^{(Q)} = 0, \tag{A-1b}$$

where Γ_{ik} is given by equation A-1a, ρ is density, and $(v^{(Q)})^2$ is the square of the phase velocity of wave type Q, where $Q = qP$, $qS1$, or $qS2$ (e.g., Musgrave, 1970; Tsvankin, 2001). For the forward problem, the wave-propagation vector direction (with components n_j and n_l) are input to A-1a, and then doing the singular value decomposition of Γ_{ik}. The resulting three eigenvalues are the phase velocities squared $(v^{(Q)})^2$ of the three wave types (Q) and the eigenvectors $A_{ik}^{(Q)}$ are their corresponding polarizations. Finally, slownesses $p^{(Q)}$, are the reciprocals of phase velocities $v^{(Q)}$.

Červený (1972, 2001) introduces an alternate definition of the Christoffel matrix as

$$G_{ik} = c_{ijkl} p_j p_l, \tag{A-2a}$$

where c_{ijkl} are density-normalized moduli, and p_j and p_l are components of the phase slowness vector. Summation over repeated indices is implied. This leads to a corresponding generalized Christoffel equation of the form (Červený, 1972)

$$G_{ik} {A_k}^{(Q)} - {A_i}^{(Q)} = 0, \tag{A-2b}$$

where the polarization vectors $\mathbf{A}^{(Q)}$ are required to be normalized, so $|\mathbf{A}^{(Q)}| = 1$, and the slowness vectors $|\mathbf{p}^{(qP)}| < |\mathbf{p}^{(qS1)}| \le |\mathbf{p}^{(qS2)}|$. As for equation A-1a above, for any given slowness vector, there are three eigenvalues and three eigenvectors, one for each of the three wave types. Here, we adopt Červený's (2001) alternate definition, as do Dewangan and Grechka (2003), and Kochetov and Slawinski (2009) for their inversions to estimate elastic tensors from polarization and slowness observations.

The Christoffel equation A-2b provides the relations between the inputs and outputs for the inversions. The inputs are the measured polarization $\mathbf{A}^{(Q)}$ and slowness $\mathbf{p}^{(Q)}$ vectors of plane qP and qS waves propagating in an anisotropic medium (calculated by the procedure described in the "Phase slowness and polarization data" subsection above, or by extraction from synthetic or field data). The outputs of the inversion are the density-normalized moduli c_{ijkl}, and in some cases, horizontal components of slownesses (e.g., Dewangan and Grechka, 2003).

APPENDIX B

THE INVERSE PROBLEM

For the inverse problem, following Dewangan and Grechka (2003), the Christoffel equation A-1a in terms of the model vector ($\mathbf{m}$) containing the elastic moduli, and the data vector ($\mathbf{d}$) containing the polarization and slowness components for each of P, qS1, and qS2 waves, can be written in the form

$$\mathbf{F}(\mathbf{m}, \mathbf{d}) = \mathbf{0}. \tag{B-1}$$

The relation between the model ($\Delta\mathbf{m}$) and data ($\Delta\mathbf{d}$) perturbations is

$$\mathbf{J}\Delta\mathbf{m} = -\mathbf{K}\Delta\mathbf{d}, \tag{B-2}$$

where

$$\mathbf{J} = \frac{\partial \mathbf{F}}{\partial \mathbf{m}}, \quad \text{and} \quad \mathbf{K} = \frac{\partial \mathbf{F}}{\partial \mathbf{d}}, \tag{B-3}$$

and $\mathbf{F}$ is given by equation A-1a. The model pertubation ($\Delta\mathbf{m}$) can be obtained by inverting matrix $\mathbf{J}$ and then, multiplying the inverse by $\mathbf{K}\Delta\mathbf{d}$ (equation B-2). $\mathbf{J}$ is a Jacobian matrix containing the first derivative of the Christoffel equation with respect to the model vector and $\mathbf{K}$ is a diagonal matrix containing the derivative of the Christoffel equation with respect to the data vector. To avoid the inversion of the nonsquare matrix $\mathbf{J}$ (the number of data are greater than the number of model parameters), the equation B-2 can be manipulated by multiplying both sides by $\mathbf{J}^{\mathrm{T}}$ to give

$$\mathbf{J}^{\mathrm{T}}\mathbf{J}\Delta\mathbf{m} = -\mathbf{J}^{\mathrm{T}}\mathbf{K}\Delta\mathbf{d}, \tag{B-4}$$

or

$$\Delta\mathbf{m} = -[\mathbf{J}^{\mathrm{T}}\mathbf{J}]^{-1}\mathbf{J}^{\mathrm{T}}\mathbf{K}\Delta\mathbf{d}. \tag{B-5}$$

Superscripts -1 and T indicate an inverse and transpose operations, respectively. Equation B-5 can be solved with any existing linearized inverse algorithm; we use the Levenberg-Marquardt algorithm (Moré, 1977), and routine lmdif from MINPACK (Moré et al., 1980) to perform the solution.

APPENDIX C

THE ELASTIC MODULI

The high-order T-matrix approach (Jakobsen et al., 2003) is used to calculate the elastic moduli. The isotropic background values of P-wave velocity (V_{P}), S-wave velocity (V_{S}), and bulk density (ρ) are 2963 m/s, 1393 m/s, and 2200 kg/m^3, respectively. All the crack sets are gas-filled (with V_{P} 300 m/s, V_{S} 0 m/s, and ρ 1.29 kg/m^3). The T-matrix crack parameters (with a crack aspect ratio of 0.05 and an aspect ratio of the crack distribution of 0.1), are the same for all crack sets. The first, second, and third crack sets have crack densities of 0.03, 0.04, and 0.02, respectively.

For clarity, each crack set is represented only by a single plane in Figure 1. The orientation of the first crack set (green) is vertical, and strikes parallel to the y-axis. The second vertical cracks (blue) have a rotation around the z-axis (ϕ) of 120°, around the x-axis (θ) of 0°, and around the y-axis (γ) of 0°. The third cracks (orange) have ϕ of 60°, θ of 30°, and γ of 45°. The reference orientation $(\phi, \theta, \gamma) = (0, 0, 0)$ is for vertical fractures parallel to the y-axis; positive rotation is counterclockwise.

The isotropic elastic moduli calculated using the host rock parameters listed above is

$$\mathbf{c} = \begin{pmatrix} 8.7795 & 4.8986 & 4.8986 & 0 & 0 & 0 \\ 4.8986 & 8.7795 & 4.8986 & 0 & 0 & 0 \\ 4.8986 & 4.8986 & 8.7795 & 0 & 0 & 0 \\ 0 & 0 & 0 & 1.9405 & 0 & 0 \\ 0 & 0 & 0 & 0 & 1.9405 & 0 \\ 0 & 0 & 0 & 0 & 0 & 1.9405 \end{pmatrix}. \quad \text{(C-1)}$$

The constructed, density-normalized triclinic moduli $\mathbf{c}$ (km^2/s^2) for creating all the noise-free synthetic examples is

$$\mathbf{c} = \begin{pmatrix} 5.5618 & 2.1916 & 2.5979 & 0.1496 & -0.0144 & -0.3308 \\ 2.1916 & 5.5145 & 2.6089 & 0.2066 & -0.0081 & -0.2901 \\ 2.5979 & 2.6089 & 6.7882 & 0.2115 & -0.0134 & -0.2240 \\ 0.1496 & 0.2066 & 0.2115 & 1.7636 & -0.0658 & -0.0011 \\ -0.0144 & -0.0081 & -0.0134 & -0.0658 & 1.7490 & 0.0392 \\ -0.3308 & -0.2901 & -0.2240 & -0.0011 & 0.0392 & 1.6588 \end{pmatrix} \quad \text{(C-2)}$$

where the indices i and j of the elements of $\mathbf{c}$ are defined using the abbreviated (two index) Voigt notation; i is the row and j is the column position of modulus c_{ij}. Negative moduli values result from the sines and cosines of the rotations of the crack planes (Helbig, 1994).

The starting model for the inversion for all the examples is the isotropic model C-1 with random noise of the form

$$c_{ij} = c_{ij} + 0.2 \times \text{randn} \quad \text{(C-3)}$$

added where randn gives normally distributed random numbers with mean zero and variance 1.0. The specific starting model that we use for inversion is

$$\mathbf{c} = \begin{pmatrix} 8.2723 & 3.9388 & 4.1757 & -0.2201 & -0.0978 & -0.2700 \\ 3.9388 & 8.1576 & 4.1647 & -0.1359 & 0.1194 & -0.2342 \\ 4.1757 & 4.1647 & 8.4074 & -0.0881 & -0.0557 & 0.0541 \\ -0.2201 & -0.1359 & -0.0881 & 2.0802 & 0.0148 & -0.2082 \\ -0.0978 & 0.1194 & -0.0557 & 0.0148 & 1.7093 & 0.0470 \\ -0.2700 & -0.2342 & 0.0541 & -0.2082 & 0.0470 & 2.2099 \end{pmatrix}. \quad \text{(C-4)}$$

The isotropic model C-1 alone or using other definitions of the added noise produce other reasonable starting models.

The elastic moduli obtained by inverting all the polarizations and vertical and horizontal components of slowness estimated from the finite-difference seismograms are

$$\mathbf{c} = \begin{pmatrix} 5.5158 & 2.1906 & 2.4586 & -0.0466 & -0.0329 & -0.3347 \\ 2.1906 & 5.4704 & 2.5002 & -0.0546 & -0.0661 & -0.3379 \\ 2.4586 & 2.5002 & 6.7561 & -0.0133 & -0.0375 & -0.2334 \\ -0.0466 & -0.0546 & -0.0133 & 1.7499 & -0.0656 & 0.0244 \\ -0.0329 & -0.0661 & -0.0375 & -0.0656 & 1.7533 & -0.0193 \\ -0.3347 & -0.3379 & -0.2334 & 0.0244 & -0.0193 & 1.6782 \end{pmatrix}. \quad \text{(C-5)}$$

Compare with the correct solution C-2.

The elastic moduli obtained by inverting all the polarizations and only the vertical components of slowness estimated from the finite-difference seismograms are

$$\mathbf{c} = \begin{pmatrix} 5.5185 & 2.1815 & 2.4570 & -0.0467 & -0.0324 & -0.3297 \\ 2.1815 & 5.4731 & 2.4972 & -0.0544 & -0.0658 & -0.3327 \\ 2.4570 & 2.4972 & 6.7561 & -0.0133 & -0.0378 & -0.2312 \\ -0.0467 & -0.0544 & -0.0133 & 1.7522 & -0.0640 & 0.0249 \\ -0.0324 & -0.0658 & -0.0378 & -0.0640 & 1.7555 & -0.0200 \\ -0.3297 & -0.3327 & -0.2312 & 0.0249 & -0.0200 & 1.6815 \end{pmatrix} \quad \text{(C-6)}$$

REFERENCES

Adam, L., 2003, Anisotropic parameter estimation from borehole data at Weyburn Field: Uncertainty and resolution: M.S. thesis, Colorado School of Mines.

Arts, R. J., and P. N. J. Rasolofosaon, 1992, Approximation of velocity and attenuation in general anisotropic rocks: 62nd Annual International Meeting, SEG, Expanded Abstracts, 640–643.

Arts, R. J., P. N. J. Rasolofosaon, and B. E. Zinszner, 1992, Complete inversion of the anisotropic elastic tensor in rocks experiment versus theory: 62nd Annual International Meeting, SEG, Expanded Abstracts, 1538–1541.

Bona, A., and M. A. Slawinski, 2008, Comparison of two inversions for elasticity tensor: Journal of Applied Geophysics, **65**, 6–9, doi: 10.1016/j.jappgeo.2008.03.002.

Burch, D. N., A. S. Calvert, and J. M. Novak, 2005, Vector fidelity of land multicomponent measurements in the context of the earth-sensor system: Misconceptions and implications: 75th Annual International Meeting, SEG, Expanded Abstracts, 904–907.

Carcione, J. M., 2007, Wave fields in real media: Elsevier.

Cerjan, C., D. Kosloff, R. Kosloff, and M. Reshef, 1985, A nonreflecting boundary condition for discrete acoustic and elastic wave equations: Geophysics, **50**, 705–708, doi: 10.1190/1.1441945.

Červený, V., 1972, Seismic rays and ray intensities in inhomogeneous anisotropic media: Geophysical Journal of the Royal Astronomical Society: **29**, 1–13.

Červený, V., 2001, Seismic ray theory: Cambridge University Press.

Chang, H., and G. A. McMechan, 2009, 3D 3-C full-wavefield inversion for estimating anisotropic parameters: A feasibility study with synthetic data: Geophysics, **74**, no. 6, WCC159–WCC175, doi: 10.1190/1.3204766.

Davis, T. L., M. J. Terrell, R. D. Benson, R. Cardona, and R. R. Kendall, 2003, Multicomponent seismic characterization and monitoring of the CO_2 flood at Weyburn Field, Saskatchewan: The Leading Edge, **22**, 696–697, doi: 10.1190/1.1599699.

Dellinger, J., D. Vasicek, and C. Sondergeld, 1998, Kelvin notation for stabilizing elastic-constant inversion: Revue de l'Institut Français du Pétrole, **53**, 709–719.

Dellinger, J. A., 1991, Anisotropic seismic wave propagation: Ph.D. dissertation, Stanford University.

de Parscau, J., and L. Nicoletis, 1990, Tranverse isotropy estimation from multioffset VSPs: 60th Annual International Meeting, SEG, Expanded Abstracts, 1439–1442.

Dewangan, P., and V. Grechka, 2003, Inversion of multicomponent, multi-azimuth, walkaway VSP data for the stiffness tensor: Geophysics, **68**, 1022–1031, doi: 10.1190/1.1581073.

DiSiena, J. P., J. E. Gaiser, and D. Corrigan, 1984, Horizontal components and shear wave analysis of three-component VSP data, *in* M. N. Toksöz and R. R. Steward, eds., Vertical seismic profiling, Part B: Advanced concepts: Geophysical Press, 177–188.

Ditri, J. J., 1994, On determination of the elastic moduli of anisotropic media from limited acoustic data: Journal of the Acoustical Society of America, **95**, 1761–1767, doi: 10.1121/1.408695.

Dongarra, J. J., C. B. Moler, J. R. Bunch, and G. W. Stewart, 1979, LINPACK User's guide: Society for Industrial and Applied Mathematics.

Gaiser, J. E., 1990, Transversely isotropic phase velocity analysis from slowness estimates: Journal of Geophysical Research, **95**, 11241–11254, doi: 10.1029/JB095iB07p11241.

Gaiser, J. E., 2003, Vector-fidelity differences between P-wave first break and PS-wave reflections: Implications for compension of full-azimuth data: 73th Annual International Meeting, SEG, Expanded Abstracts, 822–825.

Gaiser, J. E., 2007, Detector coupling corrections for vector infidelity of multicomponent OBC data: Geophysics, **72**, no. 3, V67–V77, doi: 10.1190/1.2710192.

Gomes, E., X. Zheng, I. Pšenčík, and S. Leaney, 2004, Local determination of weak anisotropy parameters from walkway VSP qP-wave data in the Java Sea region: Studia Geophysica Geodaetica, **48**, 215–231.

Grechka, V., and A. Mateeva, 2007, Inversion of P-wave VSP data for local anisotropy: Geophysics, **72**, no. 4, D69–D79.

Hardage, B. A., M. DeAngelo, and P. Murray, 2003, Defining P-wave and S-wave stratal surfaces with nine-component VSPs: The Leading Edge, **22**, 720–729, doi: 10.1190/1.1605072.

Helbig, K., 1994, Foundations of anisotropy for exploration seismics: Pergamon.

Horne, S., B. Borland, S. Ali, G. Mercado, and H. Ikawa, 2008, Anisotropic slowness inversion using 3D VSP data: 78th Annual International Meeting, SEG, Expanded Abstracts, 2947–2951.

Horne, S., and S. Leaney, 2000, Polarization and slowness component inversion for TI anisotropy: Geophysical Prospecting, **48**, 779–788, doi: 10.1046/j.1365-2478.2000.00205.x.

Hsu, K., M. Schoenberg, and J. Walsh, 1991, Anisotropy from polarization and moveout: 61st Annual International Meeting, SEG, Expanded Abstracts, 1526–1529.

Jackson, D. D., 1972, Interpretation of inaccurate, insufficient, and inconsistent data: Geophysical Journal of the Royal Astronomical Society, **28**, 97–109.

Jakobsen, M., J. A. Hudson, and T. A. Johansen, 2003, T-matrix approach to shale acoustics: Geophysical Journal International, **154**, 533–558, doi: 10.1046/j.1365-246X.2003.01977.x.

Jech, J., 1991, Computation of elastic parameters of anisotropic medium from travel times of quasi-compressional waves: Physics of the Earth and Planetary Interiors, **66**, 153–159, doi: 10.1016/0031-9201(91)90074-R.

Kendall, R., and T. L. Davis, 1996, The cost of acquiring shear waves: The Leading Edge, **15**, 943–944, doi: 10.1190/1.1437397.

Kochetov, M., and M. A. Slawinski, 2009, Estimating effective elasticity tensors from christoffel equations: Geophysics, **74**, no. 5, WB67–WB73, doi: 10.1190/1.3155163.

Leaney, W. S., and B. E. Hornby2007Depth-dependent anisotropy from subsalt walkaway VSP data: 69th Conference and Exhibition, EAGEH011.

Maultzsch, S., S. Horne, S. Archer, and H. Burkhardt, 2003, Effects of an anisotropic overburden on azimuthal amplitude analysis in horizontal transverse isotropic media: Geophysical Prospecting, **51**, 61–74, doi: 10.1046/j.1365-2478.2003.00354.x.

Menke, W., 1989, Geophysical data analysis: Discrete inverse theory: Academic Press.

Michaud, G., 2001, Time-lapse multicomponent borehole seismic monitoring of a pilot CO^2 flood: Ph.D. thesis, Colorado School of Mines.

Miller, D. E., S. Leaney, and W. H. Borland, 1994, An in situ estimation of anisotropic elastic moduli for a submarine shale: Journal of Geophysical Research, **99**, 21659–21665, doi: 10.1029/94JB01849.

Miller, D. E., and C. Spencer, 1994, An exact inversion for anisotropic moduli from phase slowness data: Journal of Geophysical Research, **99**, 21651–21657, doi: 10.1029/94JB01848.

Moré, J. J., 1977, The Levenberg-Marquardt algorithm: Implementation and theory, *in* G. A. Watson, ed., Numerical analysis: Lecture Notes in Mathematics: Springer Verlag, Volume **630**, 105–116.

Moré, J. J., B. S. Garbow, and K. E. Hillstrom, 1980, User Guide for MINPACK-1, Argonne National Laboratory Report ANL-80-74.

Musgrave, M. J. P., 1970, Crystal acoustics: Holden-Day.

Nistala, S., and G. A. McMechan, 2005, 3D modeling of fracture-induced shear-wave splitting in the Southern California Basin: Bulletin of the Seismological Society of America, **95**, 1090–1100, doi: 10.1785/0120040225.

Norris, A. N., 1989, On the acoustical determination of the elastic moduli of anisotropic solids and acoustic conditions for the existence of symmetry planes: Journal of Mechanics and Applied Mathematics, **42**, 413–426.

Ramos-Martínez, J., A. A. Ortega, and G. A. McMechan, 2000, 3-D seismic modeling for cracked media: Shear-wave splitting at zero-offset: Geophysics, **65**, no. 1211–221, doi: 10.1190/1.1444712.

Rodgers, J. L., and W. A. Nicewander, 1988, Thirteen ways to look at the correlation coefficient: The American Statistician, **42**, 59–66, doi: 10.2307/2685263.

Rusmanugroho, H., and G. A. McMechan, 2010, Modeling sensitivity of 3D, 9-C wide azimuth data to changes in fluid content and crack density in cracked reservoirs: Geophysics, **75**, no. 5, T155–T165, doi: 10.1190/1.3479555.

Tessmer, W. J., 1995, 3-D modelling of general material anisotropy in the presence of the free surface by a Chebyshev spectral method: Geophysical Journal International, **121**, 557–575, doi: 10.1111/gji.1995.121.issue-2.

Tsvankin, I., 2001, Seismic signatures and analysis of reflection data in anisotropic media: Pergamon.

van Buskirk, W. C., S. C. Cowan, and R. Carter Jr., 1986, A theory of acoustical measurement of the elastic constants of a general anisotropic solid: Journal of Materials Science, **21**, 2759–2762, doi: 10.1007/BF00551484.

Vestrum, R. W., 1994, Group- and phase-velocity inversions for the general anisotropic stiffness tensor: M.S. thesis, University of Calgary.

Winterstein, D. F., 1990, Velocity anisotropy terminology for geophysicists: Geophysics, **55**, no. 81070–1088, doi: 10.1190/1.1442919.

Xu, T., G. A. McMechan, and R. Sun, 1995, 3-D prestack full-wavefield inversion: Geophysics, **60**, 1805–1818, doi: 10.1190/1.1443913.

Zeng, X., and G. A. McMechan, 2006, Two methods for determining geophone orientations for VSP data: Geophysics, **71**, no. 4, V87–V97, doi: 10.1190/1.2208935.

Zheng, X., and I. Pšenčík, 2002, Local determination of weak anisotropy parameters from qP-wave slowness and particle motion measurements: Pure and Applied Geophysics, **159**, 1881–1905, doi: 10.1007/s00024-002-8713-z.